Detection of the melting level with polarimetric weather radar

Daniel Sanchez-Rivas and Miguel A Rico-Ramirez

Department of Civil Engineering, University of Bristol, Bristol, BS8 1TR, United Kingdom

Correspondence: Daniel Sanchez-Rivas (d.sanchezrivas@bristol.ac.uk)

Abstract. Accurate estimation of the Melting Level (ML) is essential in radar rainfall estimation to mitigate the bright band enhancement, classify hydrometeors, correct for rain-attenuation, and calibrate radar measurements. This paper presents a novel and robust ML detection algorithm based on either Vertical Profiles (VPs) or Quasi-Vertical Profiles (QVPs) built from operational polarimetric weather radar scans. The algorithm depends only on data collected by the radar itself, and it is based on the combination of several polarimetric radar measurements to generate an enhanced profile with strong gradients related to the melting layer. The algorithm is applied to one year of rainfall events that occurred over South East England, and the results were validated using radiosonde data. After evaluating all possible combinations of polarimetric radar measurements, the algorithm achieves the best ML detection when combining VPs of Z_H, ρ_{HV} and the gradient of the velocity $gradV$ whereas for QVPs, combining profiles of Z_H, ρ_{HV} and Z_{DR} produces the best results, regardless of the type of rain event. The root mean square error in the ML detection compared to radiosonde data is ~ 200 m when using VPs, and ~ 250 m when using QVPs.

1 Introduction

The Melting Level (ML) is defined as the altitude of the $0°C$ constant-temperature surface (American Meteorological Society, 2021b). It is located at the top of the melting layer, which represents the altitude interval where the transition between solid and liquid precipitation occurs (American Meteorological Society, 2021a). As the melting layer generates distinctive weather radar signatures, e.g., the well-known radar Bright Band (BB), its detection is important for meteorological and hydrological applications of weather radar rainfall measurements.

When using weather radar data for quantitative precipitation estimation (QPE), it is necessary to apply several corrections to the radar data before they can be converted into estimates of rainfall rates (Dance et al., 2019; Hong and Gourley, 2015; Mittermaier and Illingworth, 2003). For instance, corrections due to the BB are necessary as it generates a region of enhanced reflectivity due to the melting of hydrometeors, which cause an overestimation of rainfall rates (Cheng and Collier, 1993; Rico-Ramirez and Cluckie, 2007). In this case, the ML location is necessary to delimit the BB and apply algorithms that mitigate the effects of this error source in radar QPE (Sánchez-Diezma et al., 2000; Smyth and Illingworth, 1998; Vignal et al., 1999). Above the BB, a correction for the variation of the Vertical Profile of Reflectivity (VPR) is also required, especially during stratiform precipitation, where the reflectivity of snow and ice particles decreases with height. In the UK, VPR corrections to radar data are usually performed using an idealised VPR, in which the altitude of the ML is computed from a numerical weather prediction (NWP) model and assuming a constant BB thickness (Harrison et al., 2000; Mittermaier and Illingworth, 2003). Additionally, most of the radar-based hydrometeor classification algorithms require some form of separation between liquid and solid precipitation, hence the reliability of accurate identification of the ML (Hall et al., 2015; Kumjian, 2013a; Park et al., 2009). Moreover, the attenuation of the radar signal at higher frequencies (C, X, Ka and W bands) is a significant error source for radar QPE. Attenuation correction algorithms are applied in the rain region, and this requires knowledge of the height of the ML (Bringi et al., 2001; Islam et al., 2014; Park et al., 2005; Rico-Ramirez, 2012).

Knowledge of the ML is also useful to calibrate radar measurements. For instance, Z_{DR} is prone to calibration errors. The ML location is helpful to quantify the bias of Z_{DR} and mitigate errors in rain rate algorithms that use Z_H and Z_{DR} data (Richardson et al., 2017). Depending on the radar scanning strategy, radar networks worldwide have implemented operational algorithms for Z_{DR} calibration that re-

quire knowledge of the ML. Gorgucci et al. (1999) developed a method where vertical-pointing radar observations in light rain are used to calibrate Z_{DR} given that the shape of raindrops seen by the radar at 90° elevation is nearly circular and therefore Z_{DR} measurements in light rain should be around 0 dB. As vertical measurements sometimes are not available due to mechanical radar restrictions, Ryzhkov et al. (2005), Bechini et al. (2008), Gourley et al. (2009), among others, developed algorithms for Z_{DR} calibration analysing the inter-dependency between Z_{DR} and other polarimetric variables for several targets with a known -intrinsic value of Z_{DR}, e.g. rain medium or dry snow, hence the importance of the ML estimation.

There is a large number of papers that show the relationship between the BB and the melting layer. Klaassen (1988) modelled the melting layer and found that the BB enhancement in the radar reflectivity (Z_H) is related to the density of the ice particles. Fabry and Zawadzki (1995) analysed the dependency of the BB on the precipitation intensity and confirmed the relationship between the radar BB signatures and the melting of snowflakes in stratiform precipitation. White et al. (2002) introduced an algorithm based on Doppler wind profiling radar scans for detecting the BB height; their results showed a correlation between the melting layer and the peaks of the gradients of Z_H and the radial velocity (V) taken at vertical incidence. Recently, the development of polarimetric weather radar has allowed measuring the size and thermodynamic phase of precipitation particles, which has improved the identification of the melting layer. For instance, Baldini and Gorgucci (2006) used the differential reflectivity (Z_{DR}) and the differential propagation phase (Φ_{DP}) taken at vertical incidence to the analysis of the ML. They showed that the standard deviation of these measurements along with Z_H and V are useful for the identification of the ML using C-Band radar data.

Several algorithms to identify the melting layer using Range Height Indicator (RHI) scans have been proposed. Matrosov et al. (2007) proposed an approach to identify the melting layer based on ρ_{HV} (correlation coefficient) measurements collected by an X-band radar. The method relates the depressions on the ρ_{HV} profile to the melting layer, with the disadvantage that the absence of such depressions hampers the application of the algorithm. Similarly, Wolfensberger et al. (2016) designed an algorithm that combines Z_H and ρ_{HV} to create a new vertical profile that enables the detection of strong gradients related to the boundaries of the melting layer for X-band radar measurements. Their results showed that the algorithm is efficient to characterise the thickness of the melting layer. Shusse et al. (2011) described the shape and variation of the melting layer on different rainfall systems and provided insights into the behaviour of Z_{DR} and ρ_{HV} during convective precipitation using C-band radar measurements.

Algorithms to identify the melting layer based on Plan Position Indicator (PPI) scans have also been proposed in the literature. Brandes and Ikeda (2004) developed an empirical procedure based primarily on idealised profiles of Z_H, LDR and ρ_{HV} that are compared with observed profiles to estimate the height of the freezing level. The estimation of the freezing level height is refined using equations related to precipitation intensity. Giangrande et al. (2008) analysed the correspondence between maxima of Z_H, Z_{DR} and minima in ρ_{HV} to estimate the boundaries of the melting layer. This algorithm is tailored for scans with elevations angles between 4° and 10°. Later, Boodoo et al. (2010) proposed an adaptation of this algorithm, varying the scan elevation and the range of values of Z_H, Z_{DR} and ρ_{HV} making the algorithm more sensitive to less intense signatures of the melting layer. As PPIs are the most common scans derived from operational weather radars, Ryzhkov et al. (2016) proposed the Quasi-Vertical Profiles (QVPs) technique to seize the benefits of PPIs. QVPs can be used for monitoring the temporal evolution of precipitation and the microphysics of precipitation. For instance, Kaltenboeck and Ryzhkov (2017) analysed the evolution of the melting layer in freezing rain events with QVP signatures, demonstrating the ability of QVPs to represent several microphysical precipitation features as the dendritic growth layer and the riming region. Furthermore, Kumjian and Lombardo (2017), and Griffin et al. (2018) introduced new procedures for generating QVPs of the V and specific differential phase (K_{DP}) to explore the polarimetric signatures of microphysical processes in winter precipitation events at S-band frequencies. Despite the enormous benefits that QVPs bring in terms of improving our understanding of the microphysics of precipitation, there is very little research on the use of QVP-based algorithms to estimate the ML.

Most of the algorithms mentioned above require measurements often not available from operational weather radar networks as weather radars cannot always perform vertical pointing scans or produce RHI scans to observe the vertical structure of precipitation events. Hence, the main objective of this work is to present an automated, operational and robust algorithm that can accurately detect the ML based on QVPs or VPs (Vertical Profiles) collected from operational polarimetric weather radars. The algorithm outputs are validated using ML heights from high-resolution radiosonde data. Note that the proposed algorithm is not intended to replace NWP-based ML estimation methods, but it is an alternative way to detect the ML when only polarimetric weather radar measurements are available. The paper is organised as follows. Section 2 describes the datasets used to design and validate the algorithm. Section 3 examines the signatures of the melting layer on both QVPs and VPs of polarimetric variables. Section 4 provides a detailed explanation of the design of the algorithm. Results, implementation, validation and several examples of the outputs of the algorithm are presented in Section 5. Section 6 provides a discussion on the performance and implementation of the algorithm. Finally, Section 7 provides a summary of the conclusions from this work.

2 Datasets and Methods

Radiosonde data were used to validate the ML estimated from radar observations. The radiosonde is an instrument that is released into the atmosphere to measure several atmospheric parameters. The UK Met Office (UKMO) uses the Vaisala RS80 radiosonde model to collect upper-air observations twice a day at different locations across the UK. The ascent of the radiosonde extends to heights of approximately 10-30 km and take measurements at 2-second intervals (Met Office, 2007). The closest station to the selected radar site is the Herstmonceux station (see location in Figure 1), which provides high-resolution radiosonde information of pressure, temperature, relative humidity, humidity mixing ratio, sonde position, wind speed and wind direction. As these measurements provide insights for the ML location, the radiosonde data were processed to estimate the height of the $0°C$ Wet-Bulb Temperature to evaluate the algorithm performance.

The Chenies C-band operational weather radar located in South East England was selected for this work. It was one of the first UKMO radars upgraded with polarimetric capabilities (Norman et al., 2014). The radar transmits both horizontally and vertically polarised electromagnetic waves simultaneously and receives co-polar signals at the same polarisation as that of the transmitted wave, generating measurements such as Z_H, Z_{DR}, ρ_{HV} and Φ_{DP}. Radial velocity (V) measurements of the observed precipitation targets are also available; LDR measurements are also produced for the lowest elevation scan (Met Office, 2013). The volume radar scanning strategy generates different products:

- 5 PPI scans sampled on Long Pulse (LP) mode (pulse length$= 2,000\mu s$; range covered=250 km) at $0.5°$, $1°$, $2°$, $3°$ and $4°$ elevation angles with a 600 m gate resolution every 5 minutes.

- 5 PPI scans sampled on Short Pulse (SP) mode (pulse length$= 500\mu s$; range covered=115 km) at $1°$, $2°$, $4°$ $6°$ and $9°$ elevation angles, every 10 minutes and same gate resolution as above.

- One SP PPI scan at vertical incidence (range covered=12 km) every 10 minutes with 75 m gate resolution.

- One PPI scan with LDR measurements every 5 minutes at the lowest elevation ($0.5°$).

The location and other radar characteristics are provided in Table 1 and Figure 1.

Polarimetric scans related to precipitation events throughout 2018 were analysed for the design and evaluation of the algorithm. To reduce the probability of ground clutter contamination and beam spreading effects, only SP scans from the $4°$, $6°$, $9°$ and $90°$ elevations angles were retained for further processing. Then, a pre-processing of the raw-radar-data is carried out to discard non-meteorological echoes and construct the profiles of polarimetric variables:
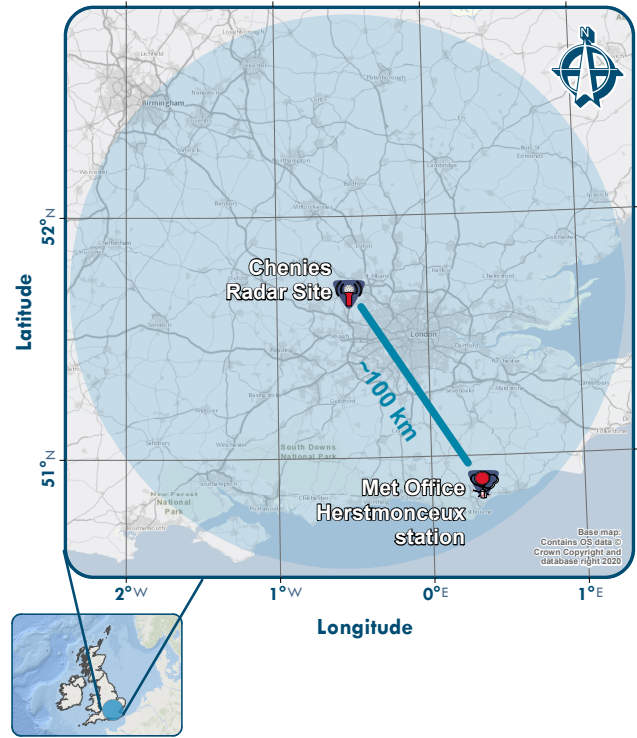
Figure 1. Location and coverage (on SP mode) of the Chenies weather radar and location of the Herstmonceux radiosonde station.

Table 1. Chenies radar characteristics.

Chenies radar	
Location	51°41'21.1"N, 0°31'46.9"W
Wavelength	$\lambda = 5.3\ cm$
Multiple elevation scans	$0.5°$ to $90°$
Beam-width	$1.0°$
Pulse Repetition Frequency	900 Hz (SP) - 300 Hz (LP)
Revolutions Per Minute	3.6 (SP) - 1.4 (LP)

- For the $4°$, $6°$ and $9°$ elevations scans, remnant clutter and anomalous propagation echoes were removed using the algorithm proposed by Rico-Ramirez and Cluckie (2008), specifically calibrated with data from this radar. Then, following the procedure suggested by Ryzhkov et al. (2016), we generated QVPs of Z_H, Z_{DR}, ρ_{HV} and Φ_{DP} measurements. The procedure suggests the azimuthal averaging of the polarimetric measurements at high elevation scans ($10°$-$30°$), but such elevation angles were not available on our datasets; hence we used the highest elevation angles available to generate the QVPs. Although it is possible to produce time-averaged QVPs to avoid local storm effects, we decided to keep the original time-resolution of the QVPs; therefore, we produced one QVP for each PPI scan. Details on the construction of the QVPs is provided in section 6.

– For the scans taken at vertical incidence, the data related to the first kilometre above ground level (a.g.l.) is not usable due to some inherent radar limitations, e.g. the de-ionisation time of the Transmit-Receive (TR) cell (Darlington, 2019, personal communication) or clutter contamination. After discarding the data below this height, an azimuthal averaging of the polarimetric and radial velocity data collected at vertical incidence was performed, generating VPs of Z_H, Z_{DR}, ρ_{HV}, Φ_{DP} and V. For the analysed radar datasets, the Spectral width variable was not available. We also define a new variable, the radial velocity gradient ($[gradV]$), computed using the gradient of the $90°$ radial velocity profile (note that $gradV \equiv dV/dH$). This new variable accentuates the profile extremes related to the change in the hydrometeor fall velocities from ice/snow to rain. The gradient of V is computed using first-order central differences in the interior points and first-order forward or backwards differences at the boundaries; for an in-depth description of numerical differentiation and finite-differences methods, see Moin (2010).

Regarding the attenuation corrections needed for Z_H and Z_{DR}, for most of the scans used in this work (especially $90°$ and $9°$ elevation scans) we observed that rain attenuation was relatively small after analysing the total differential phase shift. Furthermore, the ML height is essential to implement rain attenuation correction algorithms. Hence, no attempt was made to correct for attenuation.

Based on the constructed VPs and QVPs, a total of 94 rainfall events with visible signatures of the melting layer on Z_H or ρ_{HV} were selected, i.e. an enhancement up to 30 dBZ on Z_H or ρ_{HV} constantly decreasing below 0.90. Also, from the total number of rain events, only 25 events observed by the radar showed a suitable temporal matching with the data collected by the radiosondes, i.e. the difference in time between radar and radiosonde measurements do not exceed 2 hours. This time window was set to minimise the impact of the variability of the height of the ML.

3   Polarimetric signatures of the melting layer

The VPs and QVPs of the polarimetric measurements are displayed in Height-versus-Time plots. This enables the visualisation of the temporal evolution of the polarimetric radar signatures in the melting layer. Figure 2 depicts a stratiform rainfall event recorded between 9-10 April 2018 using VPs and QVPs ($9°$ elevation angle). It can be seen that every radar variable exhibits distinctive features that provide unique information for the identification of the melting layer on both, VPs and QVPs, e.g. Figures 2a-2b, and 2c-2d exhibit regions of enhanced values of Z_H (BB) and Z_{DR}, respectively, that are visible just below 2 km in height. Concurrently, Figures 2e-2f and 2g-2h show that ρ_{HV} and Φ_{DP}, are sensitive to the phase and shape of hydrometeors, while Figure

2i shows that the fall velocities of snow particles are lower compared to rain particles, which is an important feature that can be used to detect the ML. Figure 2j shows the gradient of the radial velocity ($[gradV]$) generated from ($90°$ elevation scans, where the BB enhancement is clearly visible at 2 km in height and it is related to the increase of the fall velocities of the hydrometeors. The different BB signatures expected in the melting layer on the QVPs and VPs are explained next.

For comparison purposes, Figure 3 shows normalised versions of VPs and QVPs (scaling each profile into the range [0, 1]) taken from the stratiform event presented in Figure 2; also, the height of the $0°C$ Wet-Bulb isotherm is shown. The normalisation process intensifies the signatures of the melting layer. Note that the QVPs provide information below 1 km; this is important for the analysis of showers or events with ML at relatively low altitude.

Given that the main objective of this work is to detect the melting layer boundaries based on the geometric features of the polarimetric profiles, herein, we will try to explain how the melting layer shapes the structure of the radar profiles. Figure 3 shows the presence of enhancements on the polarimetric profiles related to the variation of the phase and concentration of the hydrometeors. Taking the $0°C$ wet-bulb height as a reference (just below 2 km in altitude), it is feasible to associate the upper boundaries of these enhancements to the ML. These enhancements are not necessarily at the same height in all polarimetric variables, but this has to do with the backscattering properties of the melting particles and their relationship with the measured variable. Also, it is important to highlight that the methods used in the construction of the profiles play a key role in the location of the peaks, i.e. both, VPs and QVPs result from an azimuthal averaging of the rays, representing an average structure of the storm that helps to enhance the BB signature. So, the BB peaks in the VPs and QVPs in all radar measurements differ from the instantaneous profiles observed at individual slant ranges; this will be discussed in Section 6.

The reflectivity (Z_H) represents the power backscattered by precipitation particles, thus providing information about the concentration, size and phase of the hydrometeors (Hong and Gourley, 2015). In Figures 2a and 2b it can be seen that the values of Z_H on both QVPs and VPs show similar intensities. Also, the well-known BB effect on Z_H is visible on both profiles (around 1.7 km). The BB is caused by the increase in the dielectric constant of melting particles, by the change in size from large melting snowflakes to raindrops and by the increase in the fall speed of the hydrometeors that reduce the particle concentration (Fabry, 2015). The BB is easily observed in stratiform events; however, it is difficult to set the melting layer boundaries based only on Z_H, e.g. in Figure 3a the top of the BB is not easy to discern. Moreover, the profiles of Z_H do not show the BB feature in convective events; therefore, the estimation of ML for convective events based only on Z_H is not feasible.
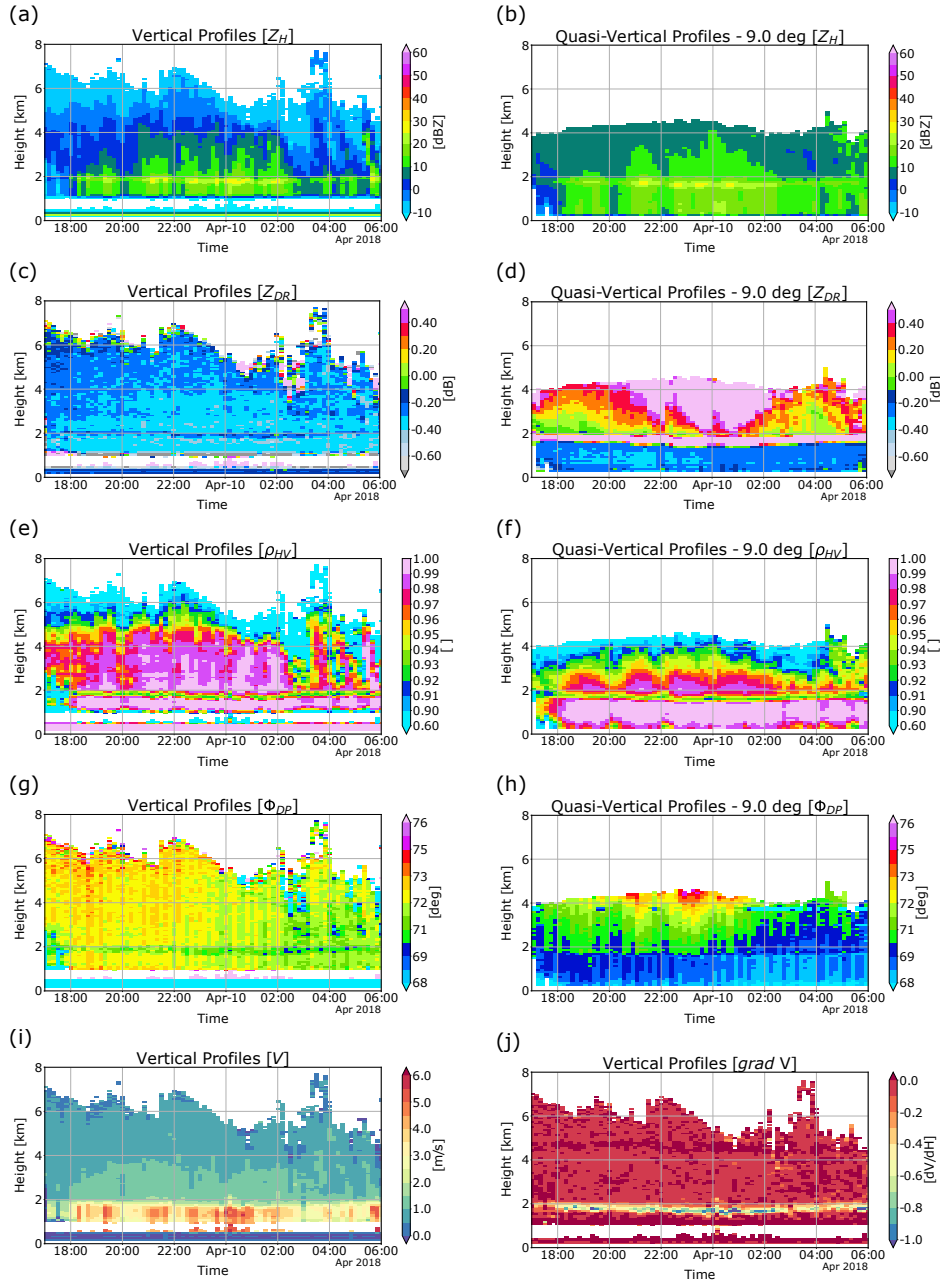
Figure 2. Height-versus-Time plots of Z_H (a-b), Z_{DR} (c-d), ρ_{HV} (e-f) and Φ_{DP} (g-h) generated from VPs (left) and QVPs (right) for a precipitation event recorded by a weather radar located at Chenies, UK. Also, (i) portrays the radial (vertical) velocity V of hydrometeors, whilst (j) shows a plot of the profiles based on the gradient of V measurements $[dV/dH]$.

The differential reflectivity (Z_{DR}) represents the ratio between horizontal and vertical reflectivity values (Z_H/Z_V) and it is related to the orientation, shape and size of the hydrometeors (Islam and Rico-Ramirez, 2014); therefore, Z_{DR} measurements for QVPs and VPs may describe different features of the particles as the elevation angle varies. For both QVPs and VPs, Z_{DR} profiles show similar behaviour in stratiform events: Figure 3b shows that Z_{DR} exhibit mean small slope changes on the rain medium (below 1.2 km), but there

is a noticeable peak associated with the melting layer on both VPs and QVPs, and although there is a difference in the peak height between both types of profiles, the top and bottom boundaries are at similar heights, especially for the QVPs. Brandes and Ikeda (2004) and Ryzhkov et al. (2016) showed that the presence of melting, randomly oriented ice particles within the melting layer and the mixing of hydrometeors produce the peaks in Z_{DR} in stratiform events. However, for profiles related to convective events (not shown), the
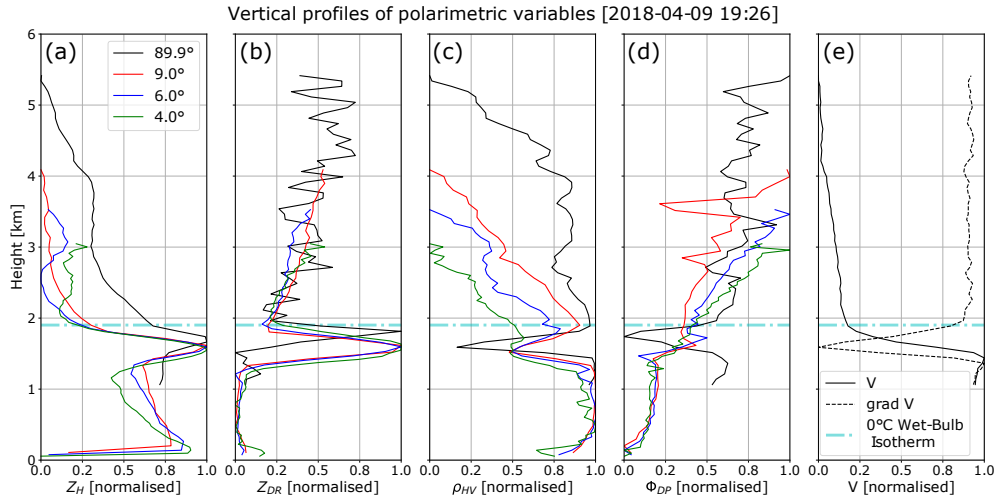
Figure 3. Normalised version of VPs and QVPs generated from polarimetric scans recorded at different elevation angles, related to a stratiform-type rain event. The $0^\circ C$ wet-bulb height is shown with the dash-dotted line.

VPs sometimes exhibit an inverse peak exactly above the rain medium and then generating a noisy, random pattern on the melting layer, that makes the estimation of the ML more difficult using VPs of Z_{DR}. Finally, the most significant difference for this variable can be seen in Figures 2c and 2d where the values of Z_{DR} for VPs and QVPs differ from each other, especially in the melting layer and above. It is also important to highlight that Z_{DR} provides valuable information for QPE. However, it usually shows a bias that must be corrected, e.g. in Figure 2c there is a bias in Z_{DR} (~ -0.35 dB) as we expect near-to-zero values for Z_{DR} in the rain region for vertically pointing measurements as raindrops are symmetrical on average when observed from underneath (Gorgucci et al., 1999). A subsequent analysis of 'birdbath' scans in light rain through the whole dataset confirmed a persistent offset in Z_{DR}. This reaffirms the importance of the detection of the melting layer boundaries, as it helps to set limits for the implementation of a Z_{DR} calibration algorithm.

The correlation coefficient (ρ_{HV}) measures the correlation between the backscatter amplitudes at vertical and horizontal polarisations. It is sensitive to the distribution of particle sizes and shapes, hence being sensitive to the hydrometeors phase, becoming a valuable hydrometeor classifier to identify non-meteorological echoes (Islam and Rico-Ramirez, 2014). Additionally, ρ_{HV} is a reliable indicator of the quality of the radar data as in the rain medium, the correlation is close to 1, becoming an indicator of the quality of the polarimetric radar measurements (Kumjian, 2013a). Figures 2e and 2f show that ρ_{HV} is close to 1 within the rain region, which confirms the high quality of this radar dataset. Figure 3c shows that the melting layer causes a similar response on ρ_{HV} as in Z_H and Z_{DR}, but in the opposite direction, resulting in a depression on the profiles starting at 1.4-1.5 km in height for QVPs and VPs, respectively. This depression results from the shift be-

tween high values of ρ_{HV}, related to raindrops and ice crystals and lower values triggered by the variety of shapes and axis ratios of the hydrometeors (Kumjian, 2013b). The behaviour of ρ_{HV} is similar on both VPs and QVPs from 9° elevation, for stratiform or convective events, where the major difference lies in the depth of the depressions. This may be caused by the resolution and elevation angle of the original scans. On the other hand, the QVPs constructed from lower elevation angles, i.e. 4° and 6° exhibit less pronounced peaks related to the melting layer and a pronounced decrease in ρ_{HV} above the BB that can make difficult to identify the ML.

As can be seen in Figures 2g, 2h, and 3d, the signatures of the melting layer on the differential propagation phase (Φ_{DP}) are, to a certain degree, ambiguous in our datasets, especially on the QVPs. Φ_{DP} represents the difference between the phase of the radar signal at horizontal polarisation and that at vertical polarisation, providing valuable information about the shape and concentration of the hydrometeors (Islam and Rico-Ramirez, 2014). Hence, the peaks on this type of profiles may be related to a greater concentration of particles due to the presence of the melting layer or the dendritic growth layer (DGL) as previously explored by Griffin et al. (2018), Kaltenboeck and Ryzhkov (2017), and Ryzhkov et al. (2016). Figure 3d shows that the QVPs of Φ_{DP} from 9° elevation exhibit a small peak at 1.7 km in height related to the melting layer but is not as pronounced as with the other polarimetric variables, although there are significant peaks aloft (between 2.8 and 3.8 km), that may represent particle (ice or snowflakes) alignment on the DGL, as suggested by Kaltenboeck and Ryzhkov (2017), while lower elevation angles do not show strong signatures on the melting layer nor the DGL. In contrast, for 90° elevation scans, there is a well-defined depression in Φ_{DP} related to melting and particle

growth (Brandes and Ikeda, 2004) at 1.8 km in height that closely matches the height of the BB; regarding the signatures of the DGL on the VPs, due to the noisiness of the profile above the ML, it is difficult to determine if these peaks
5 are related to the DGL.

Figures 2i and 3e show the profiles related to the radial (vertical) velocities (V) and the signatures of the melting layer on this variable. It can be seen that the fall velocity of the hydrometeors is relatively constant and close to zero above
10 the ML, which is related to the fall velocity of ice and snow particles, then there is a sharp increase in the fall velocity of the precipitation particles in the melting layer that becomes constant again in the rain region. However, it is challenging to incorporate the velocity profile into the ML detection be-
15 cause its features are not easy to identify using an automated peak-search algorithm. Conversely, the VP of the radial (vertical) velocity gradient ($gradV$), shown in Figures 2j and 3e (dotted line), exhibits a BB enhancement and peak similar to the rest of polarimetric variables, where the upper and lower
20 curvatures of the peak match the top and bottom extents of the melting layer.

4 Algorithm to identify the melting level

The melting level algorithm (MLA) automatically detects the ML using either QVPs or VPs, under the premise that the
25 peaks on each polarimetric profile and their curvatures are related to the melting layer. The MLA is based on the procedure proposed by Wolfensberger et al. (2016) that combines Z_H and ρ_{HV} to create a new profile with enhanced melting layer features. However, Figure 3 shows that there
30 are additional variables, such as $gradV$, that may improve the identification of the ML. Therefore, we propose an algorithm that combines all the various radar signatures to estimate the melting layer boundaries. A subsequent analysis of the outputs of the algorithm in combination with radiosonde
35 data determines the combination of radar signatures that is the best predictor of the ML. Some considerations are made for its design, e.g. to minimise the effect of beam broadening, the analysis is constrained to a height of 5 kilometres (for 9° scans, the height of the centre of the beam is similar to 30
40 km in range). Also, as shown in Figure 3, some profiles get noisy above the ML or contain spurious echoes aloft, making necessary to set an initial upper extent for the algorithm to work. The MLA is divided into two parts. The first part determines if the profile contains elements to detect the melting
45 layer based on the combination of two profiles and setting an upper limit for its implementation. The second part estimates the ML based on a combination of the polarimetric profiles and their features. The algorithm uses either QVPs or VPs, but we avoid combining both profiles as VPs might not be
50 available in other weather radar networks. A flowchart that illustrates the MLA steps is shown in Figure 4 and described below.
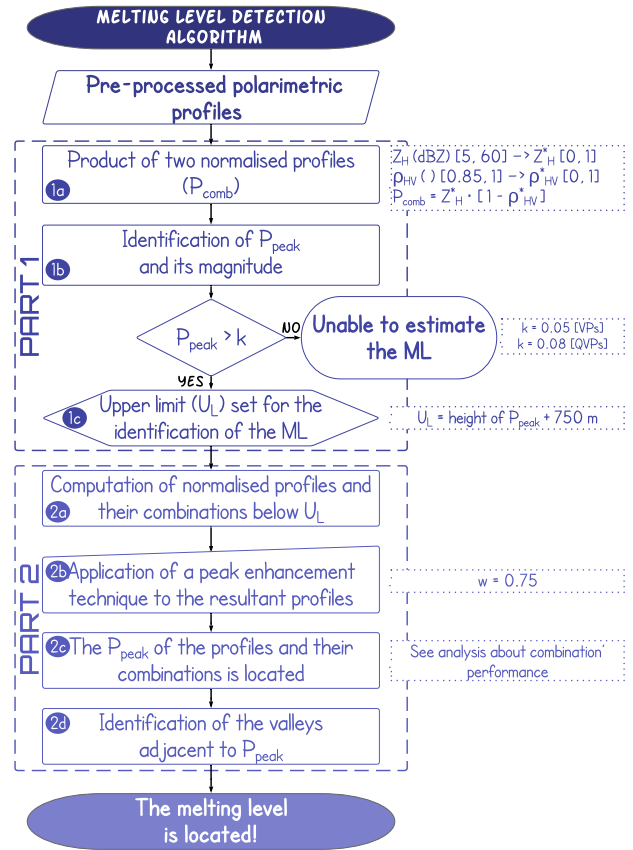
Figure 4. Flowchart of the proposed MLA.

1. **Part 1**
   The first part of the MLA identifies profiles that are likely to contain signatures related to the melting layer 55 and sets an upper limit in the profiles to use all the available variables.

1.a The algorithm takes advantage of the distinctive signatures on the profiles of Z_H and ρ_{HV} on both VPs and QVPs, to perform an initial identification 60 of rain echoes. These two profiles are normalised and combined into a single profile (P_{comb}) as suggested by Wolfensberger et al. (2016), but using different thresholds for Z_H and ρ_{HV} related to drizzle, heavy rain, snow and ice (Kumjian, 2013a; 65 Fabry, 2015). Hence, values of Z_H between 5 and 60 dBZ and ρ_{HV} between 0.85 and 1 are normalised to 0 and 1: $[Z_H(dBZ)[5, 60] \rightarrow Z_H^*[0, 1]]$ and $[\rho_{HV}(\ )[0.85, 1] \rightarrow \rho_{HV}^*[0, 1]]$. Values outside these intervals are fixed to 0 and 1, correspondingly. 70 The normalisation is carried out using the min-max normalisation procedure. Then, the normalised profiles are combined using the complement of ρ_{HV} to enhance the peaks present in the profiles:

$$P_{comb} = Z_H^* \cdot (1 - \rho_{HV}^*) \tag{1}$$ 75

Note that (*) refers to a normalised variable.

The profile P_{comb} is likely to show an enhanced peak if potential melting layer signatures were present in the profiles of Z_H and ρ_{HV}.

1.b The MLA locates the peaks on the profile P_{comb} comparing neighbouring values: a peak is a sample whose direct neighbours have smaller magnitudes. Inversely, the valleys (or boundaries of the peaks) within the profile can also be detected using a similar rationale. As several peaks can be present in the profile, the peak with the higher magnitude (i.e. the horizontal distance between the peak and the origin) is set as P_{peak}. Then, to identify profiles with a P_{peak} strong enough to be related to potential melting layer signatures, a threshold 'k' is set: if the magnitude of P_{peak} is less than the threshold k, (set to 0.05 for VPs and 0.08 for QVPs), the MLA determines that the gradients are not strong enough to correspond to melting layer signatures and therefore the profile does not contain elements to detect the ML. This step is illustrated in Figure 5a, where the magnitude of P_{peak} (~ 0.14) is greater than the threshold 'k'. Further discussion on the value of this parameter is provided in Sections 4.1 and 6.

1.c If the magnitude of P_{peak} is greater than k, an upper limit (U_L) is set taking the height of P_{peak} and adding 750 meters above. This value is selected as the melting layer thickness usually reaches values less than about 800 m (Fabry and Zawadzki, 1995); hence 750 m is sufficient to refine the search of the ML. Figure 5a illustrates this step, where 750 m are added to the height of P_{peak} (~ 1.51 km) to set an upper limit (~ 2.26km).

2. **Part 2**

In the second part of the algorithm, we incorporate the rest of the polarimetric variables to analyse its capabilities to refine the detection of the melting layer boundaries and determine the combination that better detects the ML.

2.a In this step, the profiles of all the radar variables are cut below U_L. Then, and considering that Z_H^* and ρ_{HV}^* were already normalised in step 1.a, the other variables are also normalised but using the minimum and maximum values in each profile as thresholds. To incorporate all the variables into the algorithm, the complement of the variables is used when appropriate. This is made to generate profiles with analogue peaks that enhance the footprints of the melting layer when combined with other variables. Equations 2 and 3 are derived based on the patterns observed in VPs and QVPs. These equations vary according to the combination of the vari-

ables presented in Table 2.

$$P_i^* = (1 - gradV^*) \cdot (Z_H^*) \cdot (Z_{DR}^*) \qquad (2)$$
$$\cdot (1 - \rho_{HV}^*) \cdot (1 - \Phi_{DP}^*)$$

$$P_i^* = (Z_H^*) \cdot (Z_{DR}^*) \cdot (1 - \rho_{HV}^*) \cdot (\Phi_{DP}^*) \qquad (3)$$

where i depends on the combination of the variables used according to Table 2.

The algorithm computes all the possible combinations of the profiles to analyse the influence of each variable, in this case, generating 31 different profiles if using VPs and 15 profiles when using QVPs.

2.b The profiles (P_i^*) generated in the previous step will very likely show a peak related to the melting layer. The next step in the MLA is to apply a peak-enhancement technique to refine the boundaries of this peak. This can be done using the following equation:

$$P_i = P_i^* - (w \cdot P_i^{*\prime\prime}) \qquad (4)$$

Where P_i is the enhanced profile, P_i^* is the profile given by Equations 2 or 3, w is a weighting factor and $P_i^{*\prime\prime}$ is the second derivative of P_i^*. The optimum choice of the parameter w depends upon the signal-to-noise ratio and the desirable sharpening extent. Table 2 lists the enhanced profiles produced by combining different polarimetric profiles, and Figure 5b shows the enhancement of the peak and valleys. Details on the value of the parameter w are presented in the Sections 4.1 and 6.

2.c For each profile P_i, the maximum enhancement in the BB has a magnitude given by P_{peak} and computed as in step 1.b. Then the parameter k is used to discard profiles with peaks not related to the melting layer ($k = 0.05$ for VPs; $k = 0.08$ for QVPs).

2.d The top and bottom boundaries of the BB enhancement in P_i can be placed by searching the inverse peaks (valleys) directly above and below P_{peak}. Finally, the algorithm allocates these points as the boundaries of the melting layer. This step is shown in Figure 5c, where the selected profile P_{26} is highlighted. The top valley of P_i is set as the estimated height of the ML (ML_{Top}).

As can be seen in Figure 5a, the combination of Z_H^* and $1 - \rho_{HV}^*$ produces a profile with a peak (P_{peak}) that is useful to detect the presence of the melting layer. An adequate choice of the magnitude of the parameter (k) is important to discard profiles with a P_{peak} that is not strong enough to be related to the melting layer. However, additional variables can be used (see Equations 2 and 3) to refine the detection of the ML . The upper limit (U_L) allows

Table 2. Possible combinations of polarimetric variables for VPs and QVPs used for the ML detection.

[VPs]	[QVPs]	P_1	P_2	P_3	P_4	P_5	P_6	P_7	P_8	P_9	P_{10}	P_{11}	P_{12}	P_{13}	P_{14}	P_{15}
$1-gradV^*$	-	○	○	○	○	○	○	○	○	○	○	○	○	○	○	○
Z_H^*	Z_H^*	○	○	○	○	○	○	○	●	●	●	●	●	●	●	●
Z_{DR}^*	Z_{DR}^*	○	○	○	●	●	●	●	○	○	○	○	●	●	●	●
$1-\rho_{HV}^*$	$1-\rho_{HV}^*$	○	●	●	○	○	●	●	○	○	●	●	○	○	●	●
$1-\Phi_{DP}^*$	Φ_{DP}^*	●	○	●	○	●	○	●	○	●	○	●	○	●	○	●

[VPs]	[QVPs]	P_{16}	P_{17}	P_{18}	P_{19}	P_{20}	P_{21}	P_{22}	P_{23}	P_{24}	P_{25}	P_{26}	P_{27}	P_{28}	P_{29}	P_{30}	P_{31}
$1-gradV^*$	-	●	●	●	●	●	●	●	●	●	●	●	●	●	●	●	●
Z_H^*	-	○	○	○	○	○	○	○	○	●	●	●	●	●	●	●	●
Z_{DR}^*	-	○	○	○	○	●	●	●	●	○	○	○	○	●	●	●	●
$1-\rho_{HV}^*$	-	○	○	●	●	○	○	●	●	○	○	●	●	○	○	●	●
$1-\Phi_{DP}^*$	-	○	●	○	●	○	●	○	●	○	●	○	●	○	●	○	●

Note: * refers to the normalised version of the variables.
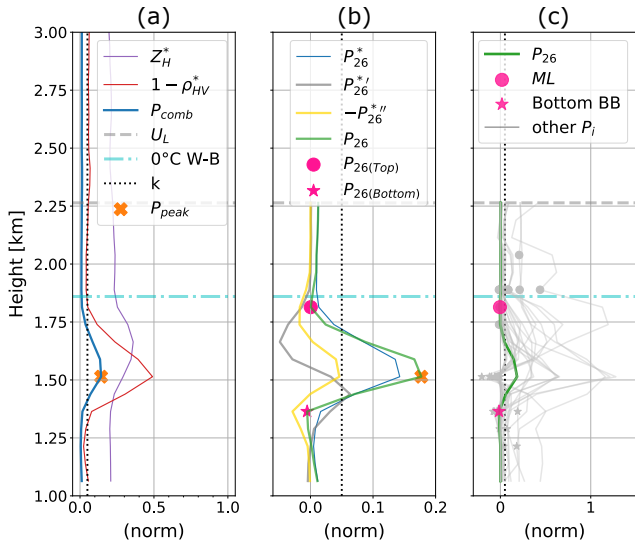
Figure 5. Depiction of the implementation of the algorithm for ML detection.

the use of other variables that otherwise could not be part of the algorithm due to noisiness or spurious echoes present at the top of the profiles. Figure 5b shows the importance of the refinement of the profile, e.g. the profile combination $P_{26}^* = (1-gradV^*) \cdot (Z_H^*) \cdot (1-\rho_{HV}^*)$ (blue line) has a peak related to the melting layer and the valley located at the top of this peak is close to the ML, but it is difficult for a peak-detection algorithm to detect its height as it is not as pronounced as required. The use of the first derivative of the profile, i.e. $P_{26}^{*\prime}$ (grey line), is not helpful as the peaks are not close to the ML. The profile P_{26} (green line) results from the implementation of Equation 4, where a value of $w = 0.75$ enhances the peak and its valleys enough for the algorithm to

detect their boundaries. A proper choice of the parameter w depends on the desired weight to the original profile rather than its second derivative. The impact of the parameters k and w on the algorithm is discussed in the following section.

4.1 Implementation of the ML algorithm

As described before, the MLA performs a pre-classification of profiles likely to contain melting layer signatures. Some tests were carried out by replacing Z_H^* with other variables (e.g. Z_{DR} or $1-gradV^*$) to identify improvements in the pre-classification. From Figure 3b, it is clear that the QVPs of Z_{DR} exhibit a pronounced peak related to the melting layer even for low elevation angles, but unfortunately Z_{DR} is not calibrated, and the thresholds for normalising this variable may vary depending on the elevation angle. On the other hand, replacing Z_H^* with the profile $1-gradV^*$ for the VPs could improve the pre-classification, but this may restrict the implementation of the algorithm, i.e. it would be only applicable if vertical velocity profiles are available. Although we observed some improvements using these variables in the first part of the MLA, especially for rain showers, we wanted to keep this part as simple and robust as possible to enable the reproducibility of the algorithm. Hence we used the combination of Z_H^* and ρ_{HV} for part 1 of the algorithm as initially proposed by Wolfensberger et al. (2016).

On the other hand, the algorithm relies on the parameters k and w, as shown in Figures 5a, and 5b. These parameters can be adjusted according to the radar datasets, e.g. the parameter k can be affected by the quality of ρ_{HV}: in our datasets and after the removal of non-meteorological echoes, ρ_{HV} exhibits values close to 0.85 in the melting layer, on both QVPs and VPs, but this may vary depending on the type of radar, scanning strategy and quality of the datasets. We set $k = 0.05$ for VPs and $k = 0.08$ for QVPs empirically, and these values

allow the algorithm to discard enhancements in the profile not related to the melting layer. Moreover, several tests were carried out using time-averaged QVPs, resulting in smoother profiles, and this parameter was helpful to identify profiles with melting layer signatures. On the other hand, Equation 4 is applied to the profiles to enhance the BB peak and the top/bottom boundaries (i.e. valleys) within the profile, thus refining the detection of the ML. This equation combines the original profile with its second derivative, weighted with the parameter w. As shown in Figure 5b, the second derivative of the profile (yellow line) exhibits deeper peaks, but its top boundary is still far from the measured ML. After several trials, we set $w = 0.75$ as this value enhances the peaks of the original profile without compromising the match of the top boundary and improving the ML detection. Likewise, this parameter can be adjusted depending on the radar datasets, e.g. profiles that exhibit smoother peaks due to the nature of its construction process and the resolution of the original scans, or profiles with vertical resolution too coarse can be adjusted with the parameter w for a better algorithm performance.

5   Results

5.1   VP and QVP comparison

Both VPs and QVPs proved to be an efficient way to monitor the temporal evolution of the melting layer, but the elevation angle used to build the QVPs affects in different ways each radar variable, as described in Section 3 and shown in Figures 2 and 3. Hence, to support the performance and outputs of the algorithm, we assessed the consistency between the Z_H profiles constructed from different elevation angles, as this is the variable less prone to significant variations due to the elevation angle. For the rest of the variables, it is not possible to compare QVPs as their characteristics vary with the elevation angle used to build the QVPs.

To carry out this analysis, we manually classified the rain events recorded by the radar according to the recommendations of Fabry and Zawadzki (1995) and Rico-Ramirez et al. (2007). From the total of 94 rainfall events, 68 events were classified as stratiform. This category includes low-level rain and rain with BB as they showed the well-known enhancement of reflectivity observed within the melting layer or look-alike drizzle events below the $0°C$. On the other hand, 26 events recorded mainly during the summer met the characteristics of showers, i.e. indistinguishable signatures of the melting layer in the Z_H profiles, in which higher values of reflectivity are present; the latter is the type of precipitation less common in the UK (Collier, 2003). The comparison between VPs and QVPs takes into account the time stamp and spatial resolution of the profiles. The Pearson correlation coefficient (r) is computed to analyse the consistency between the VPs and QVPs. The results for stratiform and convective events are shown in Figures 6 and 7, respectively.

Figure 6 shows that reflectivity values related to light and moderate rain rates (expected on stratiform-type events) are similarly depicted on both VPs and QVPs. However, the agreement diminishes when decreasing the elevation angle, mainly because higher values of Z_H do not always match their pairs as the elevation decrease. This could be explained by the averaging process carried out in the construction process of the profiles, as the radar resolution volume increases with distance. On the other hand, Figure 7 shows a more scattered distribution of Z_H for shower-type events, in which higher values of Z_H (related to moderate to heavy rain-rates) are present. Again, the correlation decreases for lower elevation angles, and it can be seen that there are mismatches for cells with higher values of reflectivity. This can be related to local storm effects and spatially nonuniform convective elements present in the QVPs, as explored by Ryzhkov et al. (2016). It is worth mentioning that QVPs constructed from lower elevation angles were also assessed (results not shown), but similar behaviour was observed, e.g. correlation decreases even further. Also, a similar analysis was carried out using other polarimetric variables. However, the results were not consistent as only Z_H describe similar properties of the precipitation measurements taken at these elevation angles.
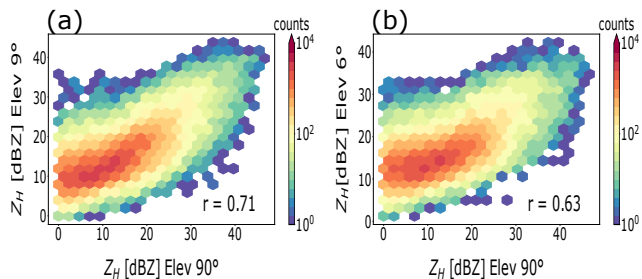
Figure 6. Comparison of VPs and QVPs of Z_H generated at two elevation angles for a collection of stratiform events. Counts indicate the number of points in the hexagon.
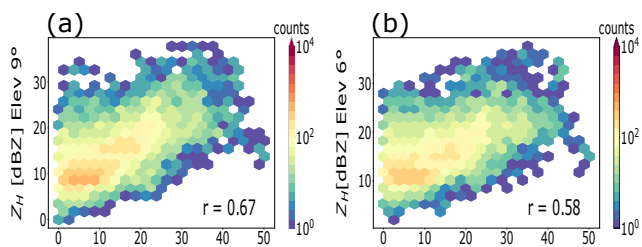
Figure 7. As in Fig. 6, but for a collection of convective events. Counts indicate the number of points in the hexagon.

5.2   ML detection from VPs

The MLA outputs were analysed to find the combination of VPs that better detects the ML. These outputs are com-

pared against $0°C$ wet-bulb isotherms over one year of rainfall events. Since soundings are released twice daily, the radiosonde data is extended at several time-steps to create short time-windows and enable a comprehensive comparison with the radar data. Performance metrics [Pearson correlation coefficient (r), Mean Absolute Error (MAE), Root Mean Square Error ($RMSE$)] between the height of the $0°C$ Wet-Bulb isotherm and the estimated ML are computed. Figure 8 shows the results for a 60-min window, i.e. the height of the $0°C$ Wet-Bulb isotherm is assumed constant 30-min before and after the time stamp of the radiosonde.
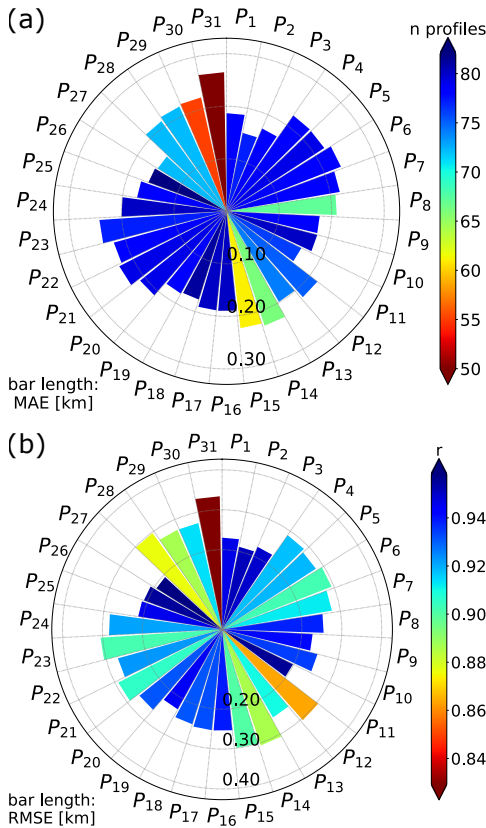
Figure 8. Errors in the ML detection for VPs using a ±30 minute window. In (a), the bar length represents the MAE (in km), and colour represents the number of vertical profiles with strong signatures detected by every polarimetric combination; in (b), the bar length represents the RMSE (in km) for every polarimetric combination and colour represents the Pearson correlation coefficient.

Figure 8 shows the capabilities of all polarimetric variables for the detection of the ML. In Figure 8a, the variable *n profiles* is an indicator of the number of profiles that, according to the algorithm, contain peaks strong enough to be related to the melting layer. This variable can only be validated by a visual inspection of the algorithm outputs, as some variables may incorrectly classify some peaks as melting-layer-related. Overall, Figure 8 shows that the combinations that include Z_H^*, $[1-\rho_{HV}^*]$ or $[1-gradV^*]$ improve the accuracy
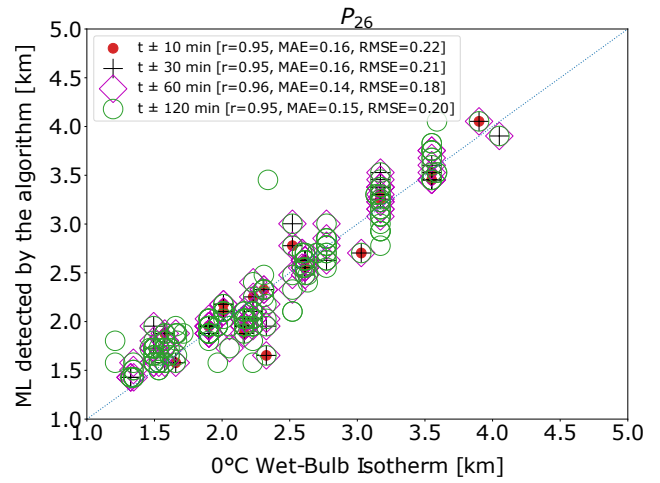
Figure 9. Heights of the $0°C$ wet-bulb isotherm versus ML detected by the algorithm using the combination P_{26} for several time windows. The 1:1 line is shown in blue. MAE and RMSE in km.
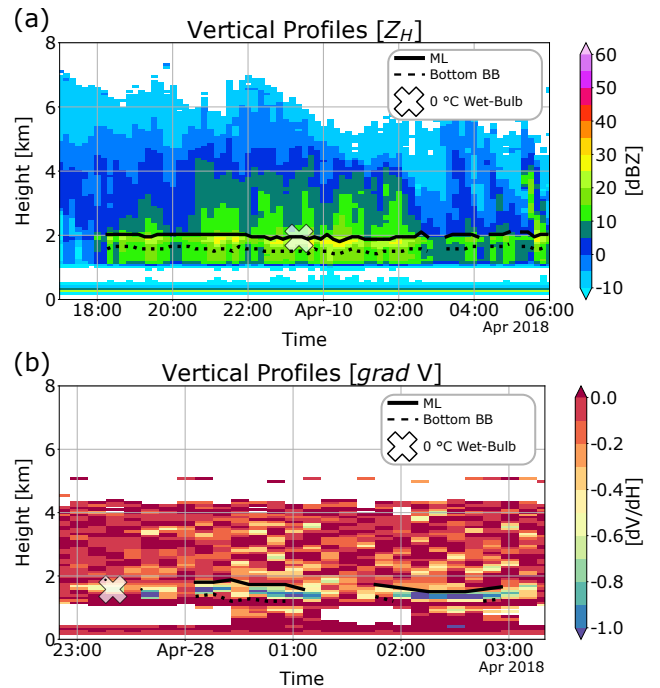
Figure 10. Comparison of the MLA outputs based on the variable P_{26} at $90°$ elevation angle for two different rain events: (a) shows the detection of the melting layer for a stratiform event displayed over a Height-versus-Time plot of Z_H, and (b) shows the performance for a convective event displayed over a Height-versus-Time plot of $gradV$.

of the MLA e.g. P_9, P_{11} or P_{26}, as the correlation and the errors are relatively low for these combinations. After a visual assessment of the performance of each combination and supported by the statistics computed above, we determine that the profile combination $P_{26} = [Z_H^* \cdot (1-\rho_{HV}^*) \cdot (1-gradV^*)]$

is the best predictor of the ML. Then, several time windows are set to assess the accuracy of the MLA over one year of radar data, as shown in Figure 9. This analysis confirms the good performance of the combination P_{26} on the ML detection, even when increasing the time window, as the $RMSE$ and MAE are close to 200 m and $r = 0.95$. Another indicator taken into account in the visual inspection of the algorithm output was the detection of the melting layer bottom and its steadiness regarding the ML. Examples of the detection of the melting layer for stratiform and convective events using the profile P_{26} are shown in Figure 10. Figures 10a and 10b, show the output of the MLA using combination P_{26} in both, stratiform or convective events. The algorithm shows a good performance, especially for stratiform events where the ML height and the rain zone are accurately defined. For the convective event, the ML is correctly identified, albeit the bottom of the melting layer is not entirely detected. This is a drawback when using the algorithm based on VPs and highlights the problems when low-altitude melting layers are present.

5.3   ML detection from QVP

The MLA is applied to QVPs generated from scans at three different elevation angles ($4°$, $6°$ and $9°$). After several trials on the parameters k and w in the algorithm implementation, only the highest elevation produced satisfactory ML estimation results. The explanation of this has its foundation in Figure 3c, where QVPs from lower elevation angles display shapes that complicate the implementation of the algorithm. For instance, the profile of ρ_{HV} exhibits a peak related to the ML, but above this peak the values of ρ_{HV} decrease sharply, whilst the profile of Z_H exhibits smoother peaks and when the normalisation process is carried out, the parameter k cannot correctly filter gradients related to the ML. Thus, after several trials and supported by the analysis presented in Section 5.1, we decided not to use the lower elevation angles ($4°$ and $6°$). Using the same windows as in the VPs, we computed several performance metrics ($r, MAE, RMSE$) between the $0°C$ wet-bulb isotherms and detected MLs. The performance of the algorithm using different profiles and a time window of 60-min (i.e. using radar profiles 30-min before and after the radiosonde timestamp) is shown in Figure 11.

Figure 11a shows that the number of profiles covered by the time window is somewhat greater than the number of profiles covered in the implementation of the VPs. This is expected because the coverage area of the PPIs from where the QVPs were constructed is greater than the vertical scans. Overall, the four indicators in Figure 11 stress the influence of Z_H and ρ_{HV} in the estimation of the ML height and reveal that adding the combination Z_{DR}^* to the analysis, i.e. P_{12}, P_{14} or P_{15} improve the delimitation of the ML, given that these combinations exhibit high values of correlation (r) and the errors are below 250 m. Based on these results, and com-
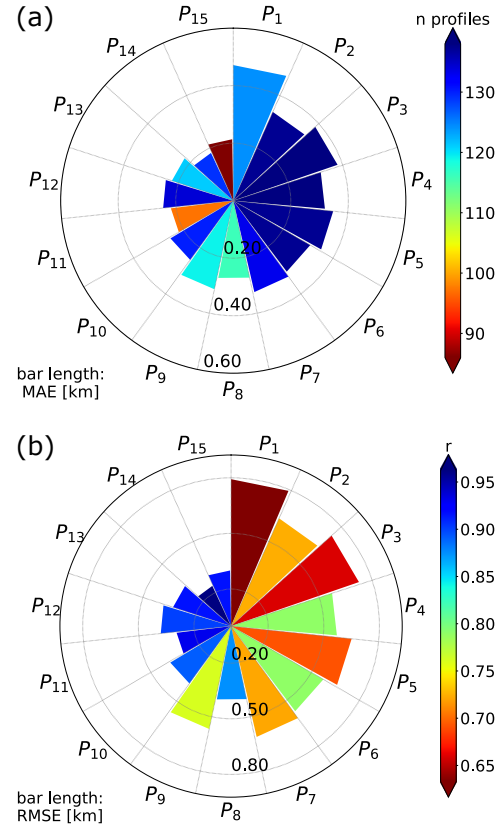
Figure 11. Errors in the ML detection for QVPs using a ±30 minute window. In (a), the bar length represents the MAE (in km), and colour represents the number of QVPs with strong signatures detected by every polarimetric combination; in (b), the bar length represents the RMSE (in km) for every polarimetric combination and colour represents the Pearson correlation coefficient.
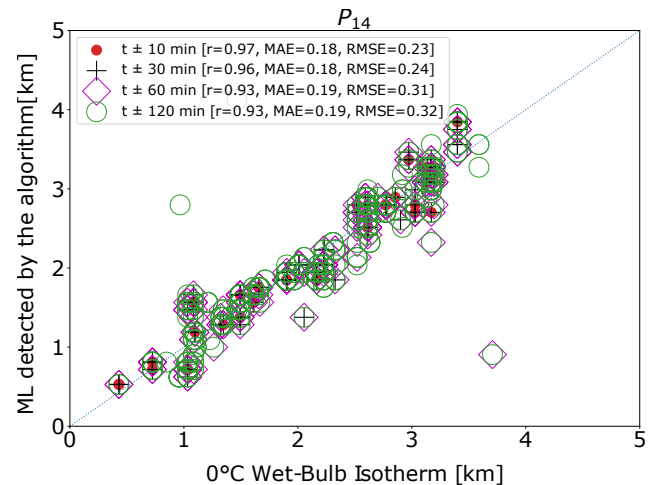
Figure 12. Heights of the $0°C$ wet-bulb isotherm versus ML estimated by the algorithm for several time windows using QVPs from $9°$ elevation scans. The 1:1 line is shown in blue. MAE and RMSE in km.

bined with a visual assessment of the outputs of the algorithm over a whole year of precipitation profiles, we concluded that the profile that combines Z_H^*, Z_{DR}^* and $(1 - \rho_{HV}^*)$, i.e. P_{14} provides the best detection of the ML. The performance of the algorithm using this combination is shown in Figure 12.

Figure 12 shows that error and correlation coefficient decrease as the time-interval increase. Given that the errors are close to 250 m for short-time windows, this combination proves to be accurate for the ML detection, making allowance for the original resolution of the scans (600 m). Two examples of the outputs of the algorithm using the profile P_{14} are shown in Figure 13 for the same stratiform and convective events as in section 5.2. The combination P_{14} shows that the ML is correctly detected, and the delineation of the rain region is well-executed. For the convective event of Figure 13b, the outputs of the algorithm are accurate for the ML estimation, although some gaps are present due to the filtering of profiles in the first part of the algorithm.
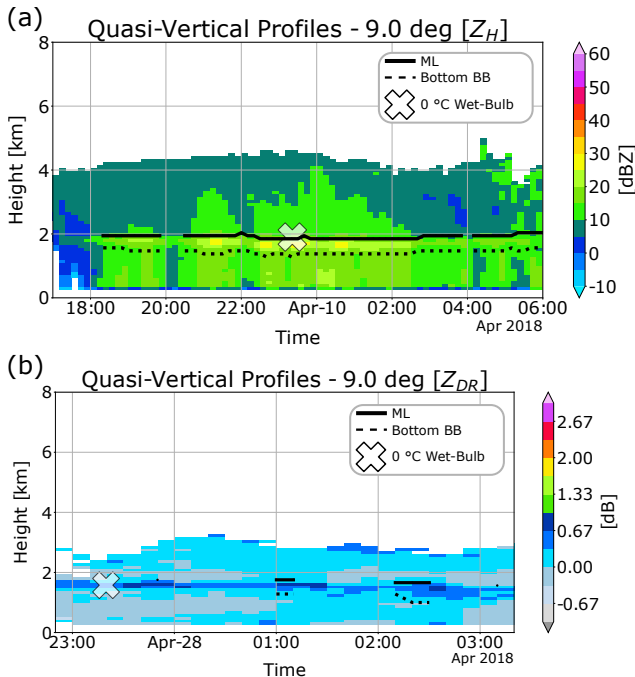
Figure 13. Comparison of the MLA outputs based on the variable P_{10} for QVPs constructed from $9°$ elevation angle scans. (a) shows the detection of the melting layer for a stratiform event displayed over a Height-versus-Time plot of Z_H; (b) shows the performance for a convective event displayed over a Height-versus-Time plot of Z_{DR}.

6   Discussion

We constructed VPs and QVPs of polarimetric variables to explore precipitation events and their features. As shown in Figure 2, both types of profiles display differences influenced by the scan elevation angle and the methods used to construct the profiles. Regarding the latter, there are several points worth discussion:

(i) It is possible to generate 'time-averaged' QVPs to smooth the effects related to local storm structures; the averaging process over the radar domain combined with temporal averaging reduces the signal noise, and it may help to discard profiles with signatures not related to the melting layer. However, the duration of the rain events and other factors raise a question about the correct time-window length. After several attempts with different time-windows, we observed that the signatures of the melting layer are often easier to discern in profiles related to stratiform events. However, for convective events, the main variables that detect the ML, e.g. Z_{DR} or ρ_{HV}, are affected by the temporal averaging, blurring the melting layer signatures. Thus, we present examples of 'instantaneous' QVPs; however, we kept in mind this matter for the MLA design;

(ii) the spatial variation of the rain events is a limitation of both VPs and QVPs. The former captures the storm structure only directly above the radar location. Even more, for the datasets used in this work, scans taken at $90°$ elevation presents limitations when reading data on the first kilometre due to technical restrictions; this situation restrains the observation of rainfall features at relative lower altitudes. On the other hand, the PPIs from where the QVPs are constructed may contain sectors with non-homogeneous echoes, e.g. a combination of mixed precipitation is possible at ranges far from the radar because the beam is considerably bigger. Moreover, at certain stages of the storm evolution, the radar echoes are insufficient to generate QVPs with clear signatures of the melting layer or even valid QVPs. This horizontal heterogeneity introduces uncertainty into the QVPs, as stated by Ryzhkov et al. (2016). These limitations on the generation of the QVPs require further investigation and are out of the scope of this work, being our main objective to detect the melting layer signatures;

(iii) due to the averaging process on the construction of the profiles, the BB shape and height do not exactly match profiles found in previous studies, especially from profiles generated from measurements collected using vertical cross-sections. For instance, Brandes and Ikeda (2004) in their Figure 1 showed that the BB peak in Z_H is higher in altitude compared to the BB peak in Z_{DR} whereas in our Figure 3a and 3b the peaks are at similar heights due to the azimuthal averaging. Our datasets show similar signatures as those shown by Brandes and Ikeda (2004) (figures not shown) when the profiles are extracted from slant ranges. Although the BB peaks are not the same in our VPs (or QVPs) due to the azimuthal averaging, the BB boundaries are on average at similar altitudes, hence not being a major problem for implementing the MLA.

After this, we analysed the different signatures of the melting layer in the VPs and QVPs. We observed that Z_H is a variable susceptible to the different types of precipitation on both VPs and QVPs, allowing the characterisation of the rain pro-

files, as previously explored by Fabry and Zawadzki (1995), Kitchen et al. (1994) and Klaassen (1988). Nevertheless, this also accentuates the trouble of detecting the ML based only on the reflectivity profiles. This emphasises the need to incorporate other polarimetric variables into the analysis.

Regarding Z_{DR}, this variable raises several questions about its potential to detect the ML. Z_{DR} is a polarimetric variable prone to calibration errors (Vivekanandan et al., 2003), and our datasets are not the exception, as shown in Figure 2c. We decided not to carry out a calibration process at this point because knowledge of the melting layer boundaries is necessary, as suggested by Gorgucci et al. (1999), Gourley et al. (2009) or Park et al. (2005). Moreover, the values of Z_{DR} vary regarding the elevation angle, as shown in Figures 2c and 2d and proved by Ryzhkov et al. (2005), where they found that Z_{DR} decrease with elevation angles for weather targets. Regardless of these drawbacks, the profiles of Z_{DR} prove to be sensitive to the hydrometeor characteristics (as shown in Figure 3b) improving the detection of the ML when using a normalised version.

On the other hand, ρ_{HV} stands out as a tell-tale of the ML, on both QVPs and VPs, as shown in Figures 2e, 2f and 3c. This agrees with the findings of Brandes and Ikeda (2004), Matrosov et al. (2007), Shusse et al. (2011) Tabary et al. (2006) or Wolfensberger et al. (2016), that included ρ_{HV} into their algorithms. Also, we analysed the quality of the radar datasets on several rain events based on this variable and found that ρ_{HV} in the rain medium is around 0.99 so the quality of this variable is reliable for further processing.

For our datasets, Φ_{DP} profiles show complex signatures that are difficult to classify, as shown in Figure 3d. Since the elevation angles used for the construction of the QVPs are below $10°$, the peaks in Φ_{DP} related to the melting layer are weak and not well defined. However, when using higher elevation angles, the peak in Φ_{DP} should increase, as shown by Trömel et al. (2014). Other peaks are also present at the top of the QVPs, but these peaks may be related to the dendritic growth layer, as explored by Kaltenboeck and Ryzhkov (2017). Additionally, the VPs of Φ_{DP} presented in Figure 3d differs from the profiles showed by Brandes and Ikeda (2004) as in their Figure 1, Φ_{DP} increase on the ML, but for our VPs, there is an inverse peak caused by the ML. Once again, this is related to the averaging process when constructing our profiles.

Finally, the vertical radial velocity V profiles prove to be a great tool to monitor the development of precipitation events as this variable describe the increase of the fall velocity of hydrometeors. Height-versus-Time plots of these profiles show an area where the velocity is nearly zero, describing the shift between ice, snow and melting particles, as shown in Figure 2i. However, it is not easy to incorporate this variable into an automated peak-detection algorithm. Hence, we propose to compute the derivative of the profile ($gradV$) as a simple but effective way to incorporate this variable into the analysis. The proposed method transforms the profile into a similar shape of the rest of the polarimetric variables to enable its incorporation into an automated peak-detection algorithm, as can be seen in Figures 2j and 3e (dotted line).

Based on the signatures triggered by the melting layer described above, we designed an algorithm that detects the strong gradients within a profile resulting from the combination of several radar measurements. The algorithm is based on the method proposed by Wolfensberger et al. (2016), but it was modified to include all the combinations of polarimetric variables and evaluate their capabilities to detect the melting layer boundaries. Also, we propose a simple method to enhance the peaks within the profiles to refine the ML detection. This method differs from previous studies where the melting layer and its boundaries are detected by complex methods that compute second-order statistics of polarimetric profiles (Baldini and Gorgucci, 2006), assume idealised profiles (Brandes and Ikeda, 2004), use a curvature detection method (Fabry and Zawadzki, 1995) or methods that rotate the coordinate system to locate the melting layer boundaries (Rico-Ramirez and Cluckie, 2007).

The results of the MLA were validated by comparing them with heights of $0°C$ wet-bulb isotherms. Using this data, we demonstrated the potential of each one of the polarimetric variables to detect the ML by presenting performance metrics of the computed profiles and their combinations, as shown in Sections 5.2 and 5.3. For the VPs, we demonstrated that the proposed profile $gradV$ is helpful for the detection of the ML (see Figure 8), especially in combination with other variables, e.g. $P_{26} = [Z_H^* \cdot (1 - \rho_{HV}^*) \cdot (1 - gradV^*)]$ accurately outlines the melting layer, regardless if it was applied to convective or stratiform events. Regarding the melting layer bottom, it is important to stress that only a visual assessment enables the validation of the performance of the algorithm on this matter, but as shown in Figure 10, the proposed variable steadily demarcates the boundaries of the melting layer. On the other hand, when applying the algorithm to QVPs, adding Z_{DR} to the analysis provided valuable information for identifying the ML. Hence the combination P_{14} is selected as the best predictor of the ML. As shown in Figure 11, the accuracy improves compared to profiles that only include Z_H^* and $1 - \rho_{HV}^*$. Also, this variable adequately delimits the melting layer, especially for stratiform events and also detects the melting layer signatures in convective events, as shown in Figure 13.

Therefore, we selected these two profiles P_{14} and P_{26} for QVPs and VPs, respectively, as the combinations that achieve the higher accuracy on the detection of the ML and, at a certain degree, the melting layer characterisation. These combinations proved to be accurate, with an average error close to the resolution of the radar and the mismatch in time and space. The proposed algorithm produces errors within 200m in the ML estimation, consistent with previous work as Brandes and Ikeda (2004); Baldini and Gorgucci (2006); Kitchen et al. (1994); Wolfensberger et al. (2016). Finally, it is worth noting that the algorithm enables the detection of the

ML based on radar measurements only, without relying on data generated from NWP model runs. This allows the implementation of radar rainfall correction schemes based on radar measurements only.

Finally, we assessed the consistency between QVPs and VPs of Z_H to ensure that the low-elevation angles available in our datasets are useful to compute reliable QVPs. Ryzhkov et al. (2016) suggested that QVPs should be built from data collected at higher elevation angles that exceed $20°$, and the results for the lower elevation angles ($4°$ and $6°$) agree with their findings, proving that decreasing the antenna elevation degrades the resolution of the QVPs. However, the QVPs collected at $9°$ elevation angles are still in good agreement with the VPs of Z_H; overall, there is a good agreement between datasets in stratiform events as the correlation coefficient is close to 0.7, but in convective events, the differences between the profiles increase, as can be seen in Figure 6 and Figure 7. Therefore, we conclude that the QVPs can be generated from elevation scans of $9°$ as the effects of beam broadening and horizontal inhomogeneity are not as pronounced as expected, and this enables the use of these QVPs of polarimetric variables for the ML detection.

7 Conclusions

In this paper, we generated QVPs and VPs of polarimetric variables collected by an operational C-band radar to explore the melting layer signatures. A long-term analysis of the VPs and QVPs revealed several findings summarised herein.

– We observed that the melting layer produces a 'fingerprint' in each of the polarimetric profiles, portraying a diversity of microphysical processes of the hydrometeors. These fingerprints (or signatures) shape the profiles in a very particular way, improving the detection of the melting layer.

– We proposed a profile $[gradV]$, generated from radial velocities taken at vertical incidence, which proved to be a helpful variable for the ML estimation.

– We performed a numerical comparison of the VPs and QVPs of reflectivity to demonstrate the consistency of the measurements involving the elevation angle of the scans. The analysis shows that QVPs generated using elevation angles at $9°$ exhibit good agreement with VPs ($r \sim 0.7$), while lower elevations increase the discrepancy between QVPs and VPs and therefore QVPs at lower elevations are not suitable for the detection of the ML.

– We developed a robust, operational MLA that detects the signatures of the melting layer using polarimetric QVPs and VPs. The fundamentals of the design of the MLA are: (i) a simple method to detect peaks and valleys within the profiles; (ii) the combination of normalised variables and (iii) the incorporation of two parameters (k and w) that can be calibrated depending on the characteristics and type of profiles.

– We showed the capabilities of all the radar variables and their combinations to detect the ML, providing individual performance metrics and analysing their performance on convective and stratiform events. For VPs, the combination P_{26}, that use the normalised version of the reflectivity, the correlation coefficient and the gradient of the velocity, i.e. $[Z_H^* \cdot (1 - \rho_{HV}^*) \cdot (1 - gradV^*)]$ achieve an accurate detection of the ML. For QVPs, the combination $P_{14} = [Z_H^* \cdot (Z_{DR}^*) \cdot (1 - \rho_{HV}^*)]$ is selected as the combination that better detects the melting layer boundaries.

– The proposed MLA proved to be accurate as the errors ($MAE, RMSE$) between the selected outputs of the MLA and the data collected by radiosonde are close to 200 m.

Code availability. The melting level detection algorithm described in this work and other radar data visualisation tools used in this study are available on request from the corresponding author.

Author contributions. Daniel Sanchez-Rivas was responsible for the development and validation of the algorithm, and writing of the paper. Miguel A Rico-Ramirez provided supervision of the work and contributed to the writing of the paper.

Competing interests. The authors declare that they have no conflict of interest.

Financial support. This research has been supported by the Mexican National Council for Science and Technology (CONACyT); and the Engineering and Physical Sciences Research Council (EPSRC), via Grant EP/I012222/1.

Acknowledgements. The authors would like to thank the UK Met Office for providing the polarimetric radar data and high-resolution radiosonde datasets through the British Atmospheric Data Centre (Met Office, 2007, 2013). This work was carried out using the computational facilities of the Advanced Computing Research Centre, University of Bristol (http://www.bris.ac.uk/acrc/). We would also like to express our gratitude to the reviewers for their constructive and positive comments.

References

American Meteorological Society: Melting layer. Glossary of Meteorology, https://glossary.ametsoc.org/wiki/Melting_layer, 2021a.

American Meteorological Society: Melting level. Glossary of Meteorology, https://glossary.ametsoc.org/wiki/Melting_level, 2021b.

Baldini, L. and Gorgucci, E.: Identification of the melting layer through dual-polarization radar measurements at vertical incidence, Journal of Atmospheric and Oceanic Technology, 23, 829–839, https://doi.org/10.1175/JTECH1884.1, 2006.

Bechini, R., Baldini, L., Cremonini, R., and Gorgucci, E.: Differential reflectivity calibration for operational radars, Journal of Atmospheric and Oceanic Technology, 25, 1542–1555, https://doi.org/10.1175/2008JTECHA1037.1, 2008.

Boodoo, S., Hudak, D., Donaldson, N., and Leduc, M.: Application of dual-polarization radar melting-layer detection algorithm, Journal of Applied Meteorology and Climatology, 49, 1779–1793, https://doi.org/10.1175/2010JAMC2421.1, 2010.

Brandes, E. A. and Ikeda, K.: Freezing-level estimation with polarimetric radar, Journal of Applied Meteorology, 43, 1541–1553, https://doi.org/10.1175/JAM2155.1, 2004.

Bringi, V. N., Keenan, T. D., and Chandrasekar, V.: Correcting C-band radar reflectivity and differential reflectivity data for rain attenuation: A self-consistent method with constraints, IEEE Transactions on Geoscience and Remote Sensing, 39, 1906–1915, https://doi.org/10.1109/36.951081, 2001.

Cheng, M. and Collier, C. G.: An Objective Method for Recognizing and Partially Correcting Brightband Error in Radar Images, Journal of Applied Meteorology, 32, 1142–1149, https://doi.org/10.1175/1520-0450(1993)032<1142:AOMFRA>2.0.CO;2, 1993.

Collier, C. G.: On the formation of stratiform and convective cloud, Weather, 58, 62–69, https://doi.org/10.1256/wea.239.02, 2003.

Dance, S. L., Ballard, S. P., Bannister, R. N., Clark, P., Cloke, H. L., Darlington, T., Flack, D. L., Gray, S. L., Hawkness-Smith, L., Husnoo, N., Illingworth, A. J., Kelly, G. A., Lean, H. W., Li, D., Nichols, N. K., Nicol, J. C., Oxley, A., Plant, R. S., Roberts, N. M., Roulstone, I., Simonin, D., Thompson, R. J., and Waller, J. A.: Improvements in forecasting intense rainfall: Results from the FRANC (Forecasting Rainfall exploiting new data Assimilation techniques and Novel observations of Convection) project, Atmosphere, 10, https://doi.org/10.3390/atmos10030125, 2019.

Darlington, T.: Met Office, (Personal communication), 2019.

Fabry, F.: Radar meteorology: principles and practice, Cambridge University Press, Cambridge, United Kingdom, 2015.

Fabry, F. and Zawadzki, I.: Long-term radar observations of the melting layer of precipitation and their interpretation, https://doi.org/10.1175/1520-0469(1995)052<0838:LTROOT>2.0.CO;2, 1995.

Giangrande, S. E., Krause, J. M., and Ryzhkov, A. V.: Automatic designation of the melting layer with a polarimetric prototype of the WSR-88D radar, Journal of Applied Meteorology and Climatology, 47, 1354–1364, https://doi.org/10.1175/2007JAMC1634.1, 2008.

Gorgucci, E., Scarchilli, G., and Chandrasekar, V.: A procedure to calibrate multiparameter weather radar using properties of the rain medium, IEEE Transactions on Geoscience and Remote Sensing, 37, 269–276, https://doi.org/10.1109/36.739161, 1999.

Gourley, J. J., Illingworth, A. J., and Tabary, P.: Absolute calibration of radar reflectivity using redundancy of the polarization observations and implied constraints on drop shapes, Journal of Atmospheric and Oceanic Technology, 26, 689–703, https://doi.org/10.1175/2008JTECHA1152.1, 2009.

Griffin, E. M., Schuur, T. J., and Ryzhkov, A. V.: A polarimetric analysis of ice microphysical processes in snow, using quasi-vertical profiles, Journal of Applied Meteorology and Climatology, 57, 31–50, https://doi.org/10.1175/JAMC-D-17-0033.1, 2018.

Hall, W., Rico-Ramirez, M. A., and Krämer, S.: Classification and correction of the bright band using an operational C-band polarimetric radar, Journal of Hydrology, 531, 248–258, https://doi.org/10.1016/j.jhydrol.2015.06.011, 2015.

Harrison, D. L., Driscoll, S. J., and Kitchen, M.: Improving precipitation estimates from weather radar using quality control and correction techniques, Meteorological Applications, 7, 135–144, https://doi.org/10.1017/S1350482700001468, 2000.

Hong, Y. and Gourley, J. J.: Radar hydrology: principles, models, and applications, Taylor & Francis, Boca Raton, 2015.

Islam, T. and Rico-Ramirez, M. A.: An overview of the remote sensing of precipitation with polarimetric radar, Progress in Physical Geography, 38, 55–78, https://doi.org/10.1177/0309133313514993, 2014.

Islam, T., Rico-Ramirez, M. A., Han, D., and Srivastava, P. K.: Sensitivity associated with bright band/melting layer location on radar reflectivity correction for attenuation at C-band using differential propagation phase measurements, Atmospheric Research, 135-136, 143–158, https://doi.org/10.1016/j.atmosres.2013.09.003, 2014.

Kaltenboeck, R. and Ryzhkov, A.: A freezing rain storm explored with a C-band polarimetric weather radar using the QVP methodology, Meteorologische Zeitschrift, 26, 207–222, https://doi.org/10.1127/metz/2016/0807, 2017.

Kitchen, M., Brown, R., and Davies, A. G.: Real-time correction of weather radar data for the effects of bright band, range and orographic growth in widespread precipitation, Quarterly Journal of the Royal Meteorological Society, 120, 1231–1254, https://doi.org/10.1002/qj.49712051906, 1994.

Klaassen, W.: Radar Observations and Simulation of the Melting Layer of Precipitation, Journal of the Atmospheric Sciences, 45, 3741–3753, https://doi.org/10.1175/1520-0469(1988)045<3741:ROASOT>2.0.CO;2, 1988.

Kumjian, M.: Principles and applications of dual-polarization weather radar. Part I: Description of the polarimetric radar variables, Journal of Operational Meteorology, 1, 226–242, https://doi.org/10.15191/nwajom.2013.0119, 2013a.

Kumjian, M.: Principles and applications of dual-polarization weather radar. Part II: Warm- and cold-season applications, Journal of Operational Meteorology, 1, 243–264, https://doi.org/10.15191/nwajom.2013.0120, 2013b.

Kumjian, M. R. and Lombardo, K. A.: Insights into the evolving microphysical and kinematic structure of northeastern U.S. winter storms from dual-Polarization doppler radar, Monthly Weather Review, 145, 1033–1061, https://doi.org/10.1175/MWR-D-15-0451.1, 2017.

Matrosov, S. Y., Clark, K. A., and Kingsmill, D. E.: A polarimetric radar approach to identify rain, melting-layer, and snow regions for applying corrections to vertical profiles of reflectivity, Journal of Applied Meteorology and Climatology, 46, 154–166, https://doi.org/10.1175/JAM2508.1, 2007.

Met Office: Met Office Herstmonceux station high resolution radiosonde data. NCAS British Atmo-

spheric Data Centre, https://catalogue.ceda.ac.uk/uuid/51b40654ef68462c818677963651a7bb, 2007.

Met Office: Chenies C-band rain radar dual polar products. NCAS British Atmospheric Data Centre, https://catalogue.ceda.ac.uk/uuid/bb3c55e36b4a4dc8866f0a06be3d475b, 2013.

Mittermaier, M. P. and Illingworth, A. J.: Comparison of model-derived and radar-observed freezing-level heights: Implications for vertical reflectivity profile-correction schemes, Quarterly Journal of the Royal Meteorological Society, 129, 83–95, https://doi.org/10.1256/qj.02.19, 2003.

Moin, P.: Fundamentals of Engineering Numerical Analysis, Cambridge University Press, Cambridge, https://doi.org/10.1017/CBO9780511781438, 2010.

Norman, K., Sugier, J., Edwards, M., Darlington, T., Lissaman, V., Riley, R., Kitchen, M., Husnoo, N., and Georgiou, S.: Renewing the UK weather radar network, in: Regional Meeting - British Hydrological Society South West Section, Bristol, 2014.

Park, H. S., Ryzhkov, A. V., Zrnić, D. S., and Kim, K. E.: The hydrometeor classification algorithm for the polarimetric WSR-88D: Description and application to an MCS, Weather and Forecasting, 24, 730–748, https://doi.org/10.1175/2008WAF2222205.1, 2009.

Park, S. G., Bringi, V. N., Chandrasekar, V., Maki, M., and Iwanami, K.: Correction of radar reflectivity and differential reflectivity for rain attenuation at X band. Part I: Theoretical and empirical basis, Journal of Atmospheric and Oceanic Technology, 22, 1621–1632, https://doi.org/10.1175/JTECH1803.1, 2005.

Richardson, L. M., Zitte, W. D., Lee, R. R., Melnikov, V. M., Ice, R. L., and Cunningham, J. G.: Bragg scatter detection by the WSR-88D. Part II: Assessment of ZDR bias estimation, Journal of Atmospheric and Oceanic Technology, 34, 479–493, https://doi.org/10.1175/JTECH-D-16-0031.1, 2017.

Rico-Ramirez, M. A.: Adaptive attenuation correction techniques for C-band polarimetric weather radars, IEEE Transactions on Geoscience and Remote Sensing, 50, 5061–5071, https://doi.org/10.1109/TGRS.2012.2195228, 2012.

Rico-Ramirez, M. A. and Cluckie, I. D.: Bright-band detection from radar vertical reflectivity profiles, International Journal of Remote Sensing, 28, 4013–4025, https://doi.org/10.1080/01431160601047797, 2007.

Rico-Ramirez, M. A. and Cluckie, I. D.: Classification of ground clutter and anomalous propagation using dual-polarization weather radar, IEEE Transactions on Geoscience and Remote Sensing, 46, 1892–1904, https://doi.org/10.1109/TGRS.2008.916979, 2008.

Rico-Ramirez, M. A., Cluckie, I. D., Shepherd, G., and Pallot, A.: A high-resolution radar experiment on the island of Jersey, Meteorological Applications, 14, 117–129, https://doi.org/10.1002/met.13, 2007.

Ryzhkov, A., Zhang, P., Reeves, H., Kumjian, M., Tschallener, T., Trömel, S., and Simmer, C.: Quasi-vertical profiles-A new way to look at polarimetric radar data, Journal of Atmospheric and Oceanic Technology, 33, 551–562, https://doi.org/10.1175/JTECH-D-15-0020.1, 2016.

Ryzhkov, A. V., Giangrande, S. E., Melnikov, V. M., and Schuur, T. J.: Calibration issues of dual-polarization radar measurements, Journal of Atmospheric and Oceanic Technology, 22, 1138–1155, https://doi.org/10.1175/JTECH1772.1, 2005.

Sánchez-Diezma, R., Zawadzki, I., and Sempere-Torres, D.: Identification of the bright band through the analysis of volumetric radar data, Journal of Geophysical Research: Atmospheres, 105, 2225–2236, https://doi.org/10.1029/1999JD900310, 2000.

Shusse, Y., Takahashi, N., Nakagawa, K., Satoh, S., and Iguchi, T.: Polarimetric radar observation of the melting layer in a convective rainfall system during the rainy season over the East China Sea, Journal of Applied Meteorology and Climatology, 50, 354–367, https://doi.org/10.1175/2010JAMC2469.1, 2011.

Smyth, T. J. and Illingworth, A. J.: Radar estimates of rainfall rates at the ground in bright band and non-bright band events, Quarterly Journal of the Royal Meteorological Society, 124, 2417–2434, https://doi.org/10.1256/smsqj.55111, 1998.

Tabary, P., Henaff, A. L., Vulpiani, G., Parent du Chatelet, J., and Gourley, J. J.: Melting layer characterization and identification with a C-band dual-polarization radar : a long-term analysis., in: Fourth European Conference on Radar in Meteorology and Hydrology, 2006.

Trömel, S., Ryzhkov, A. V., Zhang, P., and Simmer, C.: Investigations of backscatter differential phase in the melting layer, Journal of Applied Meteorology and Climatology, 53, 2344–2359, https://doi.org/10.1175/JAMC-D-14-0050.1, 2014.

Vignal, B., Andrieu, H., and Creutin, J. D.: Identification of vertical profiles of reflectivity from volume scan radar data, Journal of Applied Meteorology, 38, 1214–1228, https://doi.org/10.1175/1520-0450(1999)038<1214:IOVPOR>2.0.CO;2, 1999.

Vivekanandan, J., Zhang, G., Ellis, S. M., Rajopadhyaya, D., and Avery, S. K.: Radar reflectivity calibration using differential propagation phase measurement, Radio Science, 38, 1–14, https://doi.org/10.1029/2002rs002676, 2003.

White, A. B., Gottas, D. J., Strem, E. T., Ralph, F. M., and Neiman, P. J.: An automated brightband height detection algorithm for use with Doppler radar spectral moments, Journal of Atmospheric and Oceanic Technology, 19, 687–697, https://doi.org/10.1175/1520-0426(2002)019<0687:AABHDA>2.0.CO;2, 2002.

Wolfensberger, D., Scipion, D., and Berne, A.: Detection and characterization of the melting layer based on polarimetric radar scans, Quarterly Journal of the Royal Meteorological Society, 142, 108–124, https://doi.org/10.1002/qj.2672, 2016.